

# A Numerical Investigation of Rotating Instability in Steam Turbine Last Stage

L. Y. Zhang

e-mail: luying.zhang@eng.ox.ac.uk

L. He

e-mail: li.he@eng.ox.ac.uk

Department of Engineering Science,  
University of Oxford,  
Oxford, OX1 2JD, UK

H. Stüer

Fossil Power Generation,  
Steam, Energy Sector,  
Turbine Technology,  
Siemens AD,  
45478 Mülheim an der Ruhr,  
Germany

*The unsteady flow phenomenon (identified as rotating instability) in the last stage of a low-pressure model steam turbine operated at very low mass flow conditions is numerically studied. This kind of instability has been observed previously in compressors and can be linked to the high structural stress levels associated with flow-induced blade vibrations. The overall objective of the study is to enhance the understanding of the rotating instability in steam turbines at off design conditions. A numerical analysis using a validated unsteady nonlinear time-domain CFD solver is performed. The 3D solution captures the massively separated flow structure in the rotor-exhaust region and the pressure ratio characteristics around the rotor tip of the test model turbine stage in good comparison with the experiment. A computational study with a multi-passage whole annulus domain on two different 2D blade sections is subsequently carried out. The computational results clearly show that a rotating instability in a turbine blading configuration can be captured by the 2D model. The frequency and spatial modal characteristics are analyzed. The simulations seem to be able to predict a rotating fluid dynamic instability with the similar characteristic features to those of the experiment. In contrast to many previous observations, the results for the present configurations suggest that the onset and development of rotating instabilities can occur without 3D and tip-leakage flows, although a quantitative comparison with the experimental data can only be expected to be possible with fully 3D unsteady solutions. [DOI: 10.1115/1.4006330]*

## Introduction

To reduce power generation costs and meet environmental requirements, combined cycle power plants have been widely developed. High efficiency is required in such power plants without sacrificing long term reliability and flexibility. It brings challenges to steam turbine designs because these turbines will no longer function individually but use the steam produced by the heat from the exhaust of a gas turbine. As a result the steam turbines can face highly variable operation conditions including extreme low mass flow conditions. Such off-design conditions may cause aeroelastic problems to turbine blades, especially in the last stage of an LP turbine where the blades are relatively long and therefore vulnerable to flow induced vibrations. Since a steam turbine may undergo the part-load operation for a considerable length of time, high dynamic stresses that are associated with the blade excitation must be avoided or at least controlled to be below a certain level specified by the blade fatigue criteria. Therefore it is necessary to investigate the flow behavior of last stage LP turbines and the corresponding aero-elastic phenomena under these low mass flow off-design conditions. The mechanism understanding and predictability enhancement will enable designers to identify and reduce the risks of a mechanical failure. It is also helpful in extending the working range and improving the operational flexibility of steam turbines.

For turbomachinery blade rows operated at a low mass flow condition, self-excited unstable rotating flow patterns are often observed. However, they are mostly for the compressor/fan configurations. There are many studies of rotating stall, either in terms of understanding stall inception mechanisms, e.g., Ref. [1] or simulating the process, e.g., Refs. [2–4]. Research efforts are also made in relation to understanding acoustic characteristics of the rotating instabilities in compressors and fans at a stable operational point, e.g., Refs. [5–7]. In the context of compressors rotating instability is believed to be responsible for certain types of

excitation for rotor blade vibrations and the inception of stall and surge [8].

Recently, rotating instabilities have also been observed in turbines. An experimental study on a model turbine last stage at low mass flow conditions was conducted in the University of Stuttgart [9]. In the analysis of the measured unsteady pressure field and the relation between high amplitude disturbance and the excitation of the blades, a rotating instability was identified for the first time for turbine blade configurations. In the measured pressure signals, sharp unsteady pressure peaks were found at certain frequencies other than blade passing frequency (BPF) or its multiples. A group of small amplitude peaks were found to be evenly spaced in the main frequency humps (Fig. 1). This is a typical feature of rotating instability and suggests that some kind of rotating ‘periodic’ unsteady flow structure may be related to the pressure disturbances. Apart from the above piece of work, rotating instability in a turbine configuration has been rarely reported, little is known about the fundamental onset mechanisms, as well as whether or

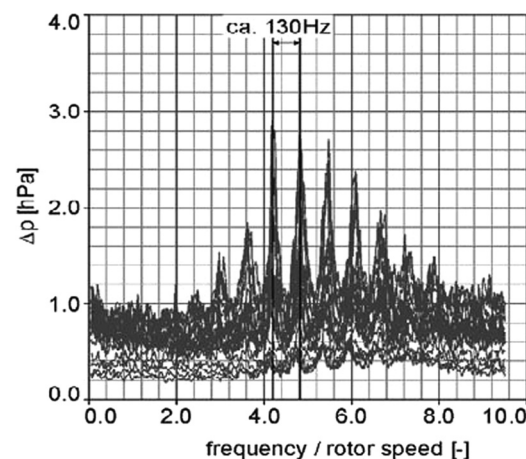


**Fig. 1** Frequency spectra of total pressure in axial gap of the last stage of a model turbine [9]

Contributed by the International Gas Turbine Institute (IGTI) of ASME for publication in the JOURNAL OF TURBOMACHINERY. Manuscript received June 24, 2011; final manuscript received August 16, 2011; published online October 22, 2012. Editor: David Wisler.

not the rotating instability in turbine is different from or similar to that in a compressor. One point worth noticing is that unlike rotating stall in compressors that may lead to a surge and complete breakdown of the flow pattern, rotating instability in steam turbines can stay in a sustainable manner at a globally stable condition. Therefore it is very important to be able to predict whether or not a rotating instability would occur and the associated blade stress level, to ensure it to be below the admissible limit.

Current understanding and conventional wisdom on rotating instabilities are largely based on the previous researches in compressors/fans. Tip clearance flow is generally regarded as being crucial to the rotating instability phenomena because pressure disturbances detected are typically prominent in the region near a blade tip. The tip clearance vortex flow is commonly considered to play a key role in forming the rotating instability structure [10,11], but the flow physics seems to be case-sensitive. Some criterion based on the tip flow characteristics was proposed for certain compressor stage configurations [12]. The nondimensional tip clearance was also considered a crucial parameter based on an experimental study [13]. In an azimuthal analysis of unsteady pressures on the casing wall of a low-speed axial-flow fan [14], rotating instability (RI) was compared with rotating stall (RS). Rotating stall is commonly characterized as an ‘almost-frozen’ flow pattern rotating circumferentially, while a rotating instability shows a fluctuating nature while rotating. A similar study [15] shows that the frequency hump of the unsteady pressures could be explained as a ‘rotating loudspeaker’: a source disturbance of one frequency in a rotating frame is able to excite pressure waves with various nodal diameters, leading to the multiple frequency peaks as observed in the fixed frame.

It is noted that so far no computational work has been reported in open literature in relation to rotating instabilities for a turbine blade configuration. The present work is motivated to identify and understand the mechanisms and basic characteristics of rotating instabilities in turbines at low mass flow conditions. A computational investigation is carried out to serve this purpose, in particular in the context of potential turbine blade aeroelastic problems, as described in the following sections.

## Numerical Method

The governing equations here are the three-dimensional Reynolds averaged Navier–Stokes equations in cylindrical coordinates  $(x, \theta, r)$  in an absolute frame of reference.

$$\begin{aligned} \frac{\partial}{\partial t} \iiint \mathbf{U} dV + \oint \left[ \mathbf{F} \cdot \mathbf{n}_x + \mathbf{G} \cdot \mathbf{n}_\theta + \mathbf{H} \cdot \mathbf{n}_r \right] dA \\ = \iiint \mathbf{S}_i dV + \oint \left[ \mathbf{F}_\nu \cdot \mathbf{n}_x + \mathbf{G}_\nu \cdot \mathbf{n}_\theta + \mathbf{H}_\nu \cdot \mathbf{n}_r \right] dA \end{aligned} \quad (1)$$

where

$$\begin{aligned} \mathbf{U} = \begin{bmatrix} \rho \\ \rho u \\ \rho v r \\ \rho w \\ \rho e \end{bmatrix}, \quad \mathbf{F} = \begin{bmatrix} \rho u - \rho u_g \\ \rho u u + P - \rho u u_g \\ (\rho u v - \rho v u_g) r \\ \rho u w - \rho w u_g \\ \rho u h - \rho e u_g \end{bmatrix}, \\ \mathbf{G} = \begin{bmatrix} \rho v - \rho v_g \\ \rho u v - \rho u v_g \\ (\rho v v + P - \rho v v_g) r \\ \rho v w - \rho w v_g \\ \rho v h - \rho e v_g \end{bmatrix}, \quad \mathbf{H} = \begin{bmatrix} \rho w - \rho w_g \\ \rho w u - \rho u w_g \\ (\rho w v - \rho v w_g) r \\ \rho w w + P - \rho w w_g \\ \rho w h - \rho e w_g \end{bmatrix}, \\ \mathbf{S}_i = \begin{bmatrix} 0 \\ 0 \\ 0 \\ \rho v^2 / r \\ 0 \end{bmatrix} \end{aligned}$$

$\mathbf{S}_i$  is the inviscid source term that accounts for the rotating effects.

$$\begin{aligned} \mathbf{F}_\nu = \begin{bmatrix} 0 \\ \tau_{xx} \\ \tau_{x\theta} r \\ \tau_{xr} \\ -q_x + u\tau_{xx} + v\tau_{x\theta} + w\tau_{xr} \end{bmatrix}, \\ \mathbf{G}_\nu = \begin{bmatrix} 0 \\ \tau_{\theta x} \\ \tau_{\theta\theta} r \\ \tau_{\theta r} \\ -q_\theta + u\tau_{\theta x} + v\tau_{\theta\theta} + w\tau_{\theta r} \end{bmatrix}, \\ \mathbf{H}_\nu = \begin{bmatrix} 0 \\ \tau_{rx} \\ \tau_{r\theta} r \\ \tau_{rr} \\ -q_r + u\tau_{rx} + v\tau_{r\theta} + w\tau_{rr} \end{bmatrix} \\ \tau_{xx} = 2\mu \frac{\partial u}{\partial x}, \quad \tau_{\theta\theta} = 2\mu \left( \frac{1}{r} \frac{\partial v}{\partial \theta} + \frac{w}{r} \right), \quad \tau_{rr} = 2\mu \frac{\partial w}{\partial r} \\ \tau_{r\theta} = \tau_{\theta r} = \mu \left( \frac{1}{r} \frac{\partial w}{\partial \theta} - \frac{v}{r} + \frac{\partial v}{\partial r} \right) \\ \tau_{xr} = \tau_{rx} = \mu \left( \frac{\partial u}{\partial r} + \frac{\partial w}{\partial x} \right), \quad \tau_{x\theta} = \tau_{\theta x} = \mu \left( \frac{\partial u}{r \partial \theta} + \frac{\partial v}{\partial x} \right) \end{aligned}$$

where  $(u_g, v_g, w_g)$  are moving grid velocities. If the mesh is rotating in an angle velocity of  $\Omega$ , as the case often seen in the rotor row of turbomachinery, then the moving grid velocity is  $(0, \Omega r, 0)$ .

The Spalart–Allmaras one-equation turbulence transport model is adopted [16]. For the solid wall surface, the slip wall condition is applied with the shear stresses being evaluated from the log law so that a coarser mesh can be used to reduce computing time. For inlet and exit boundaries, the boundary condition for the steady flow solutions (specifying inlet stagnation pressure, stagnation temperature, inlet flow angle, and exit static pressure) is adopted. At the circumferential boundaries of a multiblade passage domain a direct periodic boundary condition is implemented.

The spatial discretization for the equations is the second-order cell-centered finite volume scheme. The fluxes are calculated from the flow variables at the cell surface. The summation is taken along the boundary surfaces. Second and fourth-order adaptive smoothing is used to suppress numerical oscillations [17]. The time-marching solution is performed by four-stage Runge–Kutta integration, accelerated by a time-consistent or connectivity based multigrid techniques [18]. In a multiblade row, calculation meshes are fixed to the stator or rotor blades and patched at the interface. Local instantaneous information is transferred directly across the interface by a second-order interpolation method [18].

## Steady Flow Validation

In the current study, the time-domain nonlinear time marching solver is used for a steady flow first as a baseline solution. A low-speed 2D LP turbine blade sections in a linear cascade with large scale flow separation on the pressure side is calculated as a test case. The surface pressures for this case were measured in the corresponding experiment [19]. In the calculations, the blade is scaled up by a factor of 2.3. The computational mesh for this cascade is O-mesh with the total mesh points of 46,338 for 5 blocks in a single-passage domain.

Figure 2 shows the steady pressure distributions along the blade surface compared with the experimental data, for the inlet flow angle of 20 deg. This inflow angle corresponds to a negative

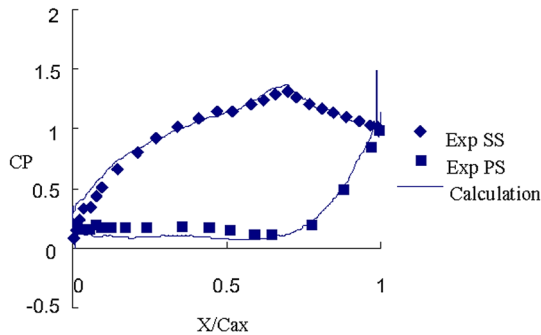


Fig. 2 Steady pressures compared with experiment [19] (inlet flow angle 20 deg, Reynolds number 220,000)

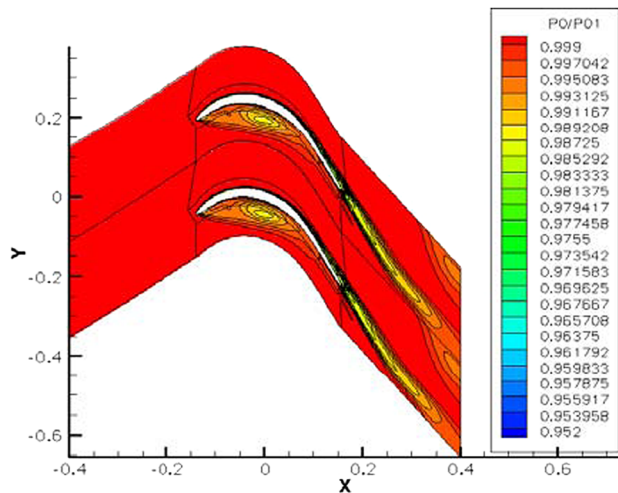


Fig. 3 Contours of steady total pressures

incidence of around 20 deg. The comparison with the experiment shows good agreement. From the computational result of the stagnation pressure loss contours (Fig. 3) the large scale pressure surface separation can be clearly observed. The boundary layer on the pressure side separates from the leading edge and reattaches at a position over half the axial chord. The calculation captures the flow separation and surface pressure very well for this case. The flow physics is similar to the case of the last-stage rotor blades at low mass flow rate conditions, where a low axial flow velocity and a constant rotating speed lead to a high negative incidence angle for the rotor and thus a massive separation on the pressure surface.

### Model Turbine Stage (3D Solutions)

The model turbine stage tested in the University of Stuttgart [9,20] which exhibits the rotating instabilities is investigated here. To reduce the computational cost we make an approximation of the blade count ratio to 2:3, which means 2 stators and 3 rotors passages in the computational domain. The rotor row rotates at a frequency of 210 Hz. A 3D calculation at the design condition is conducted first as a baseline. The results are compared with those from a well-established 3D time-marching RANS code [21] using the mixing plane method for multistage simulations. The results show a good overall agreement in the basic stage aerothermal performance parameters between the two codes.

To further simulate the conditions in the experiment [20], calculations for the last stage of the model turbine are carried out with a diffuser attached, as shown in Fig. 4. A flow separation takes place in the diffuser behind the rotor row in the experiment

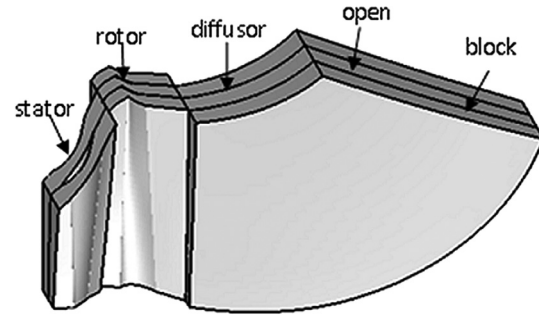
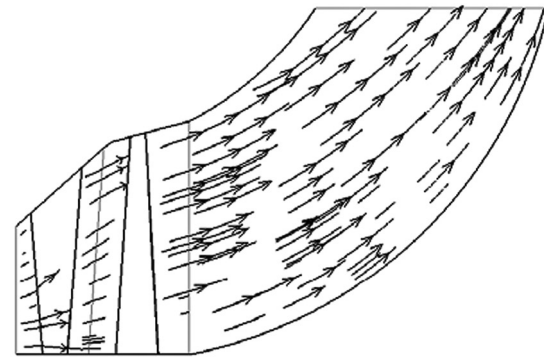
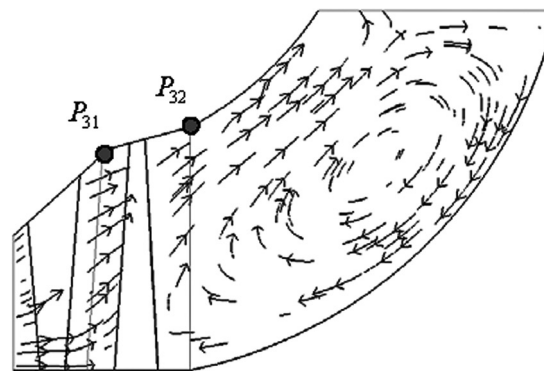


Fig. 4 Computational domain of the model turbine stage (2 stator passages, 3 rotor passages)



a) Nominal condition



b)  $\phi_r = 0.258$

Fig. 5 Calculated streamlines in the model turbine stage

(Fig. 6). To more effectively control flow conditions and capture the flow separation in the diffuser, the exit of the diffuser is partially blocked in the computations. A multipassage H-mesh domain is adopted and  $37 \times 93 \times 46$  mesh points are used for each stator passage;  $37 \times 111 \times 46$  mesh points are used for each rotor passage and  $37 \times 100 \times 46 \times 3$  mesh points in total are used for the diffuser. A direct periodic boundary condition is adopted at the circumferential boundaries of the multipassage domain. Tip clearance is not included in the current study.

Figure 5 shows the calculated streamlines in the turbine stage. The flow pattern at the off-design condition (Fig. 5(b)) is dramatically changed from the case at the nominal condition (Fig. 5(a)), especially in the diffuser part. The separated flow structure behind the rotor is well captured by the calculation (comparing Fig. 5(b)



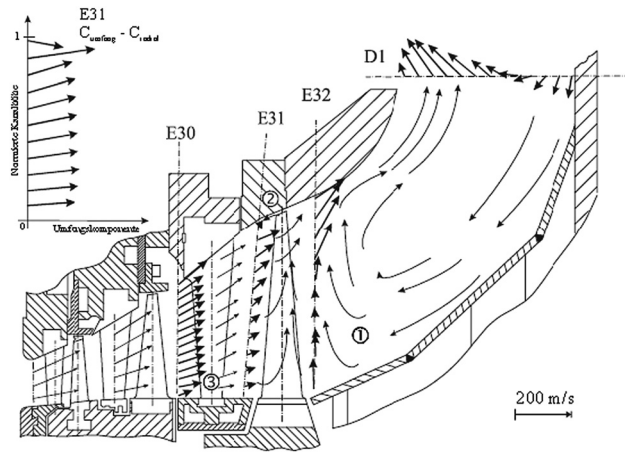


Fig. 6 Experimental flow patterns. ( $\phi_r = 0.22$ ) [20].

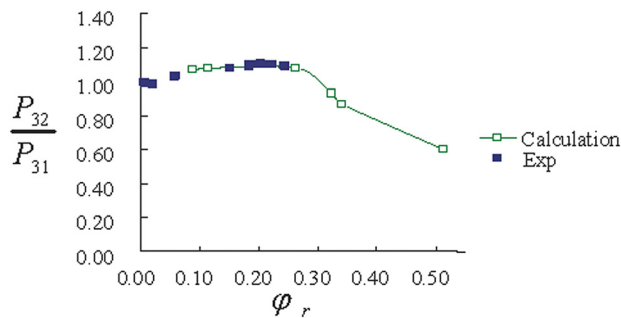


Fig. 7 Calculated rotor tip pressure ratio compared with the measurement [20]. ( $P_{31}$  and  $P_{32}$  are taken from the locations shown in Fig. 5(b).)

with Fig. 6). A big vortical structure with the massive flow separation is formed near the hub. In the experiment the reverse flow goes from the exit of the diffuser to the exit of the rotor row and affects the flow angle in the rotor row (Fig. 6). This feature is also well captured by the calculation (Fig. 5(b)).

In the experiment, the casing pressures were measured before and after the rotor blade row (denoted as  $P_{31}$ ,  $P_{32}$ , respectively, in Fig. 5(b)) for a range of flow conditions. Several operation conditions with low volume flow rates are considered in the calculations to provide the baseline flow characteristics. The calculated casing static pressure ratios across the rotor blade row are compared with the measured results at various operating conditions in Fig. 7. The calculation shows a good agreement with the measurement at off-design low flow conditions. At a relative volume flow rate less than 26% of the design condition, the ratio between the exit static pressure and the inlet static pressure of the rotor tip becomes higher than 1, which means the tip region of the turbine rotor blade now functions as a compressor. Meanwhile, the overall turbine stage can still keep working persistently in a stable manner without a global reverse flow which would otherwise result in a complete breakdown of stage performance as in a compressor surge.

Although the off-design conditions are simulated and the massive separation is well captured in the 3D calculations, no rotating instability is observed from the 3D computational results so far. It is suspected to be due to the rather limited computational domain in the circumferential direction. The wavelength of the circumferential nonuniformity is restricted by the periodic boundary condition. For the 3D simulations, the computational domain only contains 2 stator passages and 3 rotor passages, which is considered not large enough.

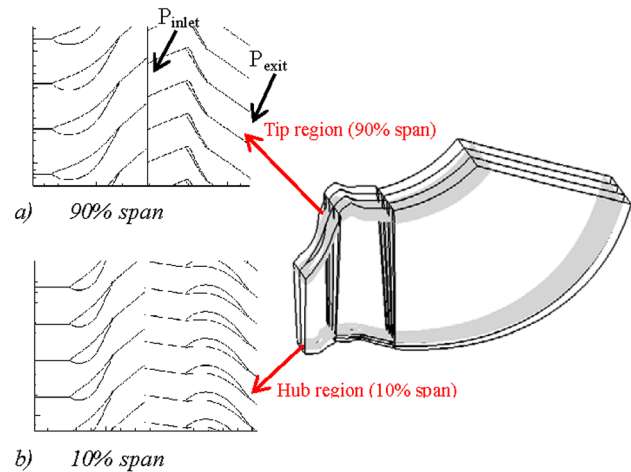


Fig. 8 2D multipassage configurations

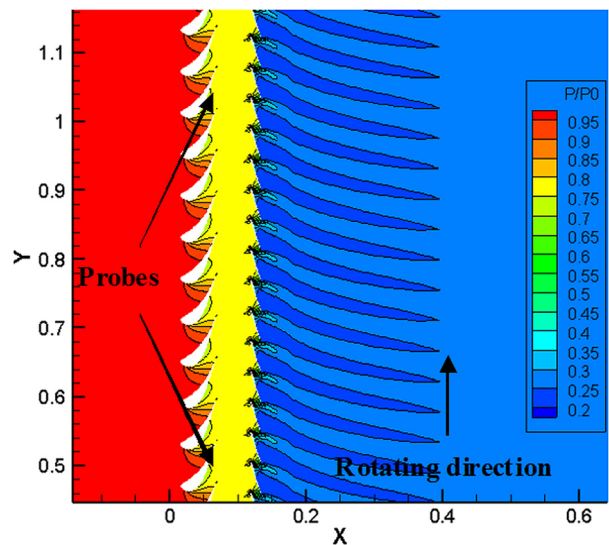


Fig. 9 Static pressure contour on 90% span section (nominal flow condition, 100%)

## Rotating Instability in 2D Configuration

**Setup of Computational Domain of 2D Sections.** As 3D whole annulus unsteady calculations are highly time-consuming, a first attempt to study the rotating instabilities is made on 2D whole annulus multipassage configurations. The aim is to help to gain some fundamental understanding on the onset mechanism of rotating instabilities in turbines. Although 3D flow effects such as those due to tip leakage are often regarded as essential for the onset of a rotating instability in compressors, it is of interest to examine what might and can happen in a pure 2D configuration. In this respect, 2D calculations should provide a reference case before considering the tip clearance flow and other 3D effects.

Two 2D configurations are taken in the computations. Blade profiles from the near hub (10% span) and near tip (90% span) sections are considered, respectively (Fig. 8). A uniform condition is set at the inlet. The nominal flow condition and off-design low mass-flow conditions are obtained by changing the outlet static pressures.

**Analysis of Rotating Instability (Near Tip Section).** Figure 9 shows the static pressure contours on the near tip plane at the nominal flow condition. Flow throughout the stage reveals a clear passage-passage periodicity, subject only to the expected rotor-

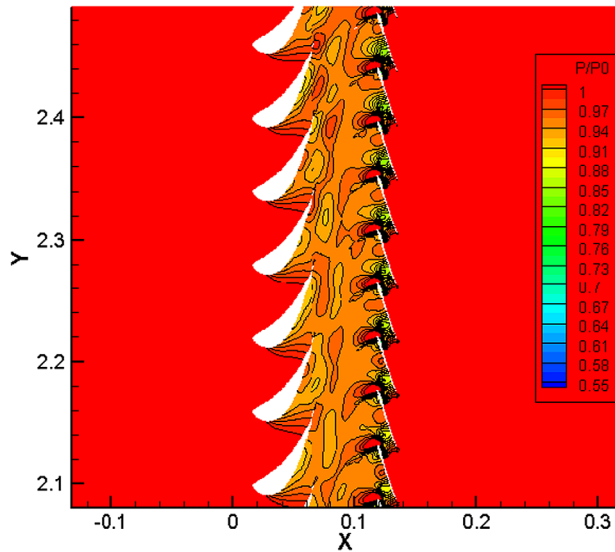


**Fig. 10** Static pressure contours on 90% span section (relative flow rate: 71.2%)

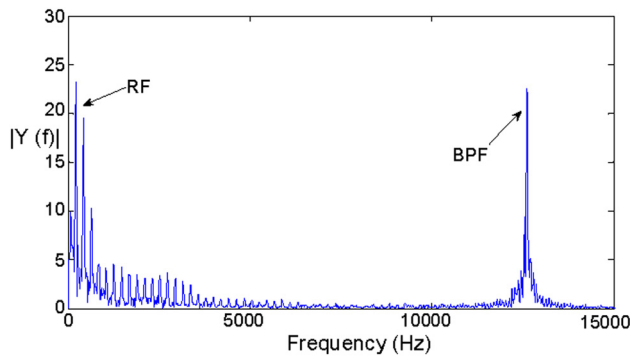


**Fig. 11** Frequency spectra (90% span section) of unsteady pressures (relative mass flow rate: 74.8%)

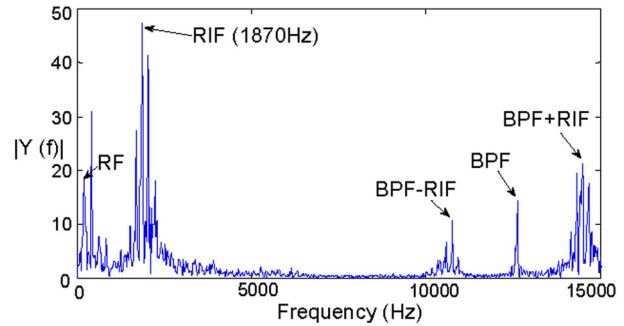
stator bladerow interactions. No nonsynchronized unsteadiness is detected at the nominal condition.

For a low mass flow condition, a large blockage is originated from the pressure side separation. The separated vortical flow structures appear to be unstable and are shed in a non-synchronized manner in rotor passages. A clear circumferential nonuniformity starts to appear, as shown in Fig. 10. These disturbance structures rotate and evolve across the annulus and result in large amplitude pressure fluctuations throughout the stage.

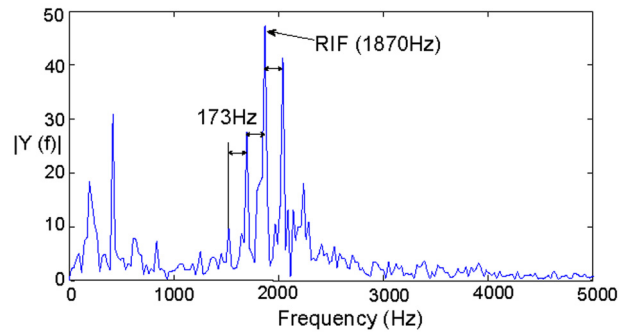
Several numerical probes are placed in the stator middle passage positions immediately downstream of the stator trailing edge (Fig. 9). The time traces of the unsteady pressures at these probe points are taken to give the Fourier spectra in the frequency domain (Figs. 11–13). The unsteady pressure signals from the probes show different frequency patterns for different relative mass flow rates.

At a relatively high mass flow rate (74.8% of the nominal), no instability is triggered. The disturbances which can be observed from the frequency spectra are only those of blade passing frequency (BPF), rotor rotating frequency (RF) and its multiples (Fig. 11).

When the relative mass flow rate is decreased to 72.7%, a distinctively different spectrum appears (Fig. 12). A group of peaks are found with a dominant frequency at about 1870 Hz, which is not synchronous with either BPF or RF. This frequency is consid-



*a) Overall Spectrum (0-15000 Hz).*



*b) Close-up (0-5000 Hz).*

**Fig. 12** Frequency spectra (90% span section) of unsteady pressures (relative mass flow rate: 72.7%)

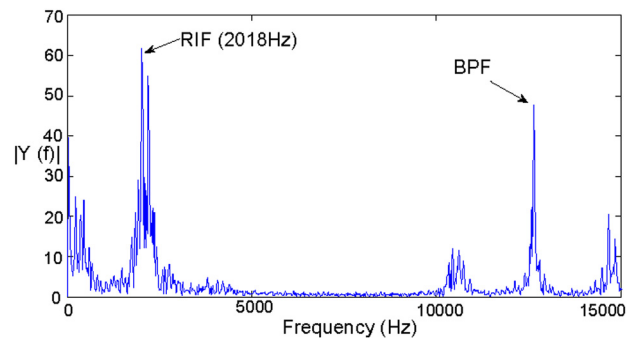


**Fig. 13** Frequency spectra (90% span section) of unsteady pressures (relative mass flow rate: 71.2%)

erably higher than the rotating instability frequency (RIF) in the experiment [9], which is about 1000 Hz. It needs to be pointed out that the flow rate here is normalized by the local 2D reference value, which may well be different from the condition in the 3D configuration. Taking these into consideration, the results are not directly comparable to the experimental data. The finding is nevertheless interesting. The broadband hump is superimposed with evenly spaced peaks (Fig. 12(b)), which is similar to the rotating instability frequency pattern in the experiment (Fig. 1). In addition, the largely constant interval between adjacent frequency peaks is about 173 Hz, while in the experiment the frequency interval is about 130 Hz. Tonal components at difference cross-coupled subharmonic frequencies such as  $(BPF \pm RIF)$  are also visible. The blade passing disturbances shown by BPF are not prominent now compared with the magnitude of the rotating instability unsteadiness (RIF).

When the mass flow rate is further decreased to 71.2% of the nominal flow rate, the amplitude of the instability (RIF) signal gets much stronger (Fig. 13). In addition, the dominant frequency shifts to a higher frequency (about 2018 Hz) now (Table 1).

**Table 1 Rotating instability frequency versus relative flow rate**

Relative mass flow rate	Dominant R.I. frequency (Hz)
74.8%	NA
72.7%	1870
71.2%	2018
70.4%	2067

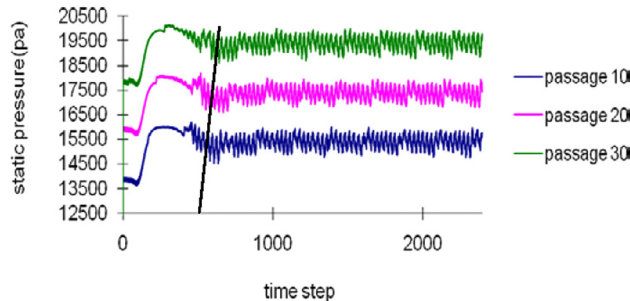
**Fig. 14 Time traces of static pressures of 90% span section (relative mass flow rate: 65.6%)**

Figure 14 shows the time traces of the unsteady pressure signals taken from three stator passages. The absolute value of the pressures for passage 10 and 20 are shifted by  $-4000$  Pa and  $-2000$  Pa, respectively, for clarity of the presentation. The rotating instability is triggered during the initial transient. It shows the pressure fluctuations with amplitudes over  $1000$  Pa. The disturbances stay within a stable range (i.e. in a limit cycle pattern) that will not lead to a global flow breakdown as in a surge for a compressor system. There are phase differences between the time traces of the three passages. Passage 10 is leading passage 20 and passage 30. This means that relative to the stator, the flow pattern moves in the same direction as the rotation of the rotor.

**Modal Analysis of Rotating Instability (Near Tip Section).** An effort is also made to identify the circumferential wave patterns in terms of the numbers of the circumferential nodes and the rotational speed. A modal analysis is carried out for the relative mass flow rate of  $70.4\%$ . The frequencies of rotating disturbance in an absolute (stator) or a relative (rotor) frame of reference can be described as [13],

$$\omega_A = \omega_R + n \cdot \Omega \quad (2)$$

$$\Omega = 210 \text{ Hz}$$

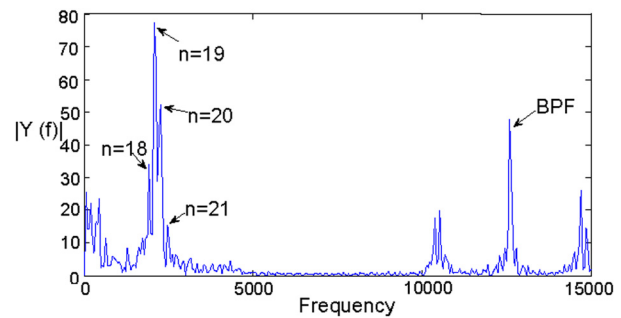
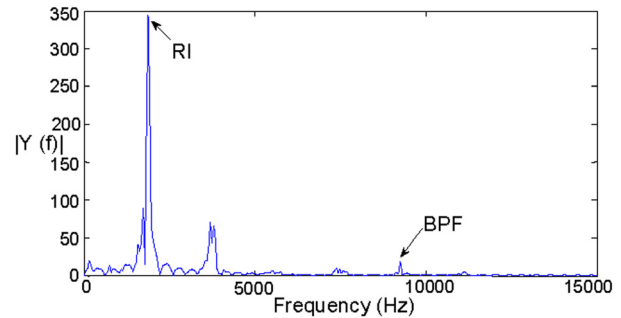
$$n = \frac{|\omega_A| \pm |\omega_R|}{\Omega} \quad (3)$$

where  $\omega_A$  is the frequency measured in the absolute frame of reference (in Hz);  $\omega_R$  is the frequency measured in the relative one (in Hz),  $\Omega$  is the rotational speed of the rotor (in Hz), and  $n$  is the node number (equivalent to the number of nodal diameters).

The frequency spectrum from the stator frame of reference shows a group of rotating instability pressure peaks over a range of frequencies (Fig. 15). It indicates the disturbance source is able to excite pressure waves with various nodal diameters. In the frame of the moving source, i.e., the rotating instability frame of reference, the frequency  $\omega_{RI}$  can be related to  $\omega_A$  by [14]:

$$\omega_{A,n} = \omega_{RI} + n \cdot \Omega_A \quad (4)$$

$$\omega_{A,n+1} = \omega_{RI} + (n+1) \cdot \Omega_A \quad (5)$$

**Fig. 15 Frequency spectra from stator frame of reference (90% span, relative mass flow rate: 70.4%)****Fig. 16 Frequency spectra from rotor frame of reference (90% span, relative mass flow rate: 70.4%)****Table 2 Peak frequencies in different frames of reference**

Frequency (Hz)	Peak 1	Peak 2	Peak 3	Peak 4	$\Omega$
$n$	18	19	20	21	
$\omega_{A,n}$ (absolute)	1920 Hz	2067 Hz	2264 Hz	2461 Hz	189.5 Hz ( $\Omega_A$ )
$\omega_{R,n}$ (relative)	1870 Hz	1870 Hz	1870 Hz	1870 Hz	20.5 Hz ( $\Omega_R$ )
$\omega_{RI}$ (rotating instability)	1405 Hz	1405 Hz	1405 Hz	1405 Hz	

$$\Delta\omega_{A,\Delta n=1} = \Omega_A \quad (6)$$

$$\Omega_A \approx 189.5 \text{ Hz}$$

$$\Omega_A = \Omega + \Omega_R \quad (7)$$

$$\Omega_R \approx -20.5 \text{ Hz}$$

where  $\Omega_A$  is the rotating speed of the traveling source in the absolute frame of reference and  $\Omega_R$  is the speed seen in the rotor relative frame of reference. As such, both the mode orders and the traveling speed of the source can be deduced by the frequency spectrums from the stator frame of reference (Fig. 15) and the rotor frame of reference (Fig. 16). The main peak frequencies are shown in Table 2.

The main node numbers identified from the frequency peaks in Figs. 15 are 18, 19, 20, 21. The absolute rotating speed of the disturbance sources is about  $189.5$  Hz, which is about  $90.2\%$  of the rotor speed. In the rotor frame of reference the instability sources are moving at  $20.5$  Hz but in the opposite direction to that of the rotation. The overall characteristics are quite similar to those in the experiments [9].

**Examination of Mesh Sensitivity.** For the rotating instabilities obtained from the 2D computations described above, a relevant question can be asked regarding the mesh dependence: to what

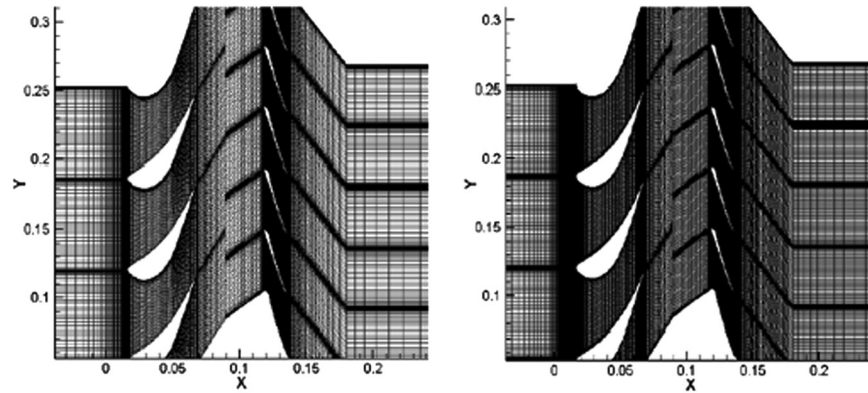


Fig. 17 Computational meshes (90% span) (left: original; right: refined)

Table 3 Mesh densities for 2D configurations (90% span)

Number of grids	Original		Refined	
	Stator	Rotor	Stator	Rotor
Streamwise	121	136	181	204
Pitchwise	37	37	55	55
In total (per passage)	4477	5032	9955	11,220

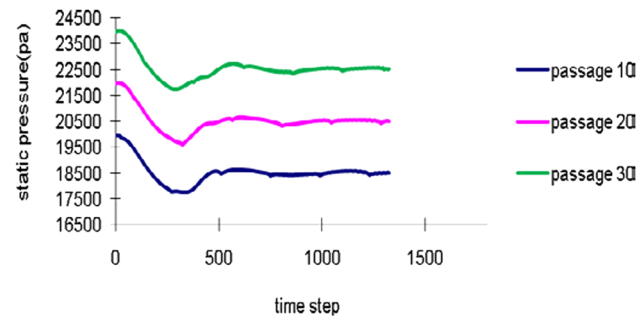


Fig. 19 Time traces of static pressures of 10% span section (relative mass flow rate: 14.7%)

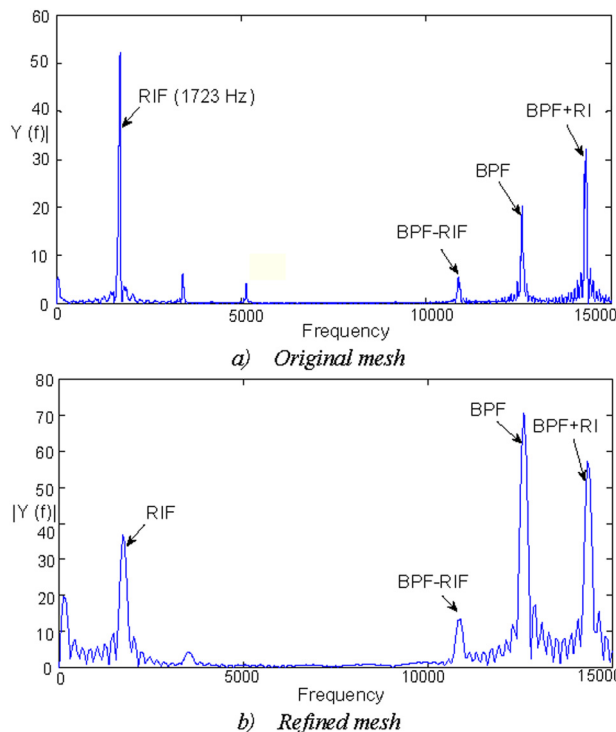


Fig. 18 Frequency spectra (90% span) of unsteady pressures from two meshes (relative mass flow rate: 70.4%)

extent may these calculated rotating instabilities be dependent on the mesh density? It is important that the observed rotating instability behavior is qualitatively independent of mesh density. Two meshes of different densities (Fig. 17) are adopted to examine the mesh dependency of the calculations for the blade tip section. The details of the meshes are in Table 3. For the purposes of the present mesh-dependence study, a smaller computational domain containing 4 stator passages and 6 rotor passages is adopted here. The original mesh has the same mesh density per passage as in the full annulus calculations shown in Figs. 9 and 10.

The rotating instability is also identified in the smaller domain calculations at a relative mass flow rate of 70.4%. The frequency spectra from the original mesh and the refined mesh capture the same main frequency peaks for the RIF, BPF and the cross-coupled subharmonic frequencies (Fig. 18). This mesh dependency study shows that the original mesh density adopted is sufficient to capture consistently the main characteristics of the rotating instability.

**Analysis of Near-Hub Section.** Now we turn the attention to the near hub section (10% span). The results of the near hub section are quite different from those of the near tip section. The hub section seems much more resistant to a rotating instability development at a low mass flow rate. Even when the mass flow rate is decreased to 14.7% of the nominal value, no noticeable rotating instability is detected (comparing Fig. 21 with Fig. 10). The time traces of static pressures in the three stator passages (with a constant shift for passage 10 and 20) are shown in Fig. 19. In a clear contrast to the counterpart for the near tip section (Fig. 14), the hub results show no clearly identifiable fluctuations. The only peaks visible in the corresponding frequency spectra are at BPF and frequencies near zero which is due to the very slow changes in the mean pressures (Fig. 20).

With the rotor blade profile near the hub having a high camber (Fig. 8(b)), it tends to have a large separation on the pressure side with a high blockage (Fig. 22). However, the high camber blading also seems to localize the effects of the separated zone and reduce the likelihood of forming a circumferential synchronized rotating disturbance. Thus an unstable rotating flow pattern seems to be more difficult to develop around the annulus near the hub.

**Further Discussion on Near-Tip and Near-Hub Sections.** Some further points should be noted regarding the stage blading profiles at the two spanwise sections. Firstly, the stator



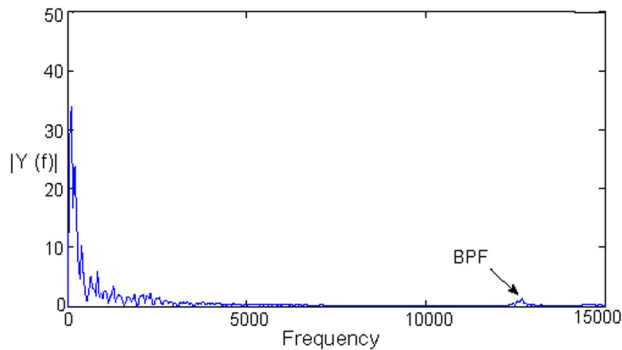


Fig. 20 Frequency spectra (10% span section) of unsteady pressures (relative mass flow rate: 14.7%)

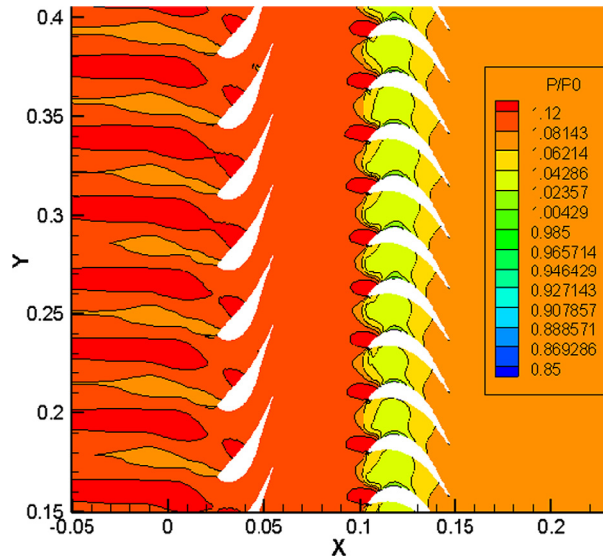


Fig. 21 Pressure contours on 10% span section (relative flow rate: 14.7%)

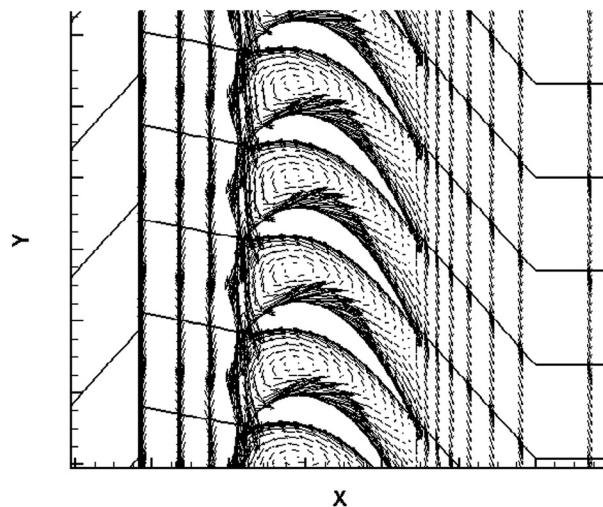


Fig. 22 Relative velocity vectors on 10% span section (relative flow rate: 14.7%)

blading for the two sections look quite similar, but the rotor profiles are very different (Fig. 8). The blading profile of the rotor tip section shows some similarity to a supersonic fan blade profile. The rotor blade shape for the near hub section

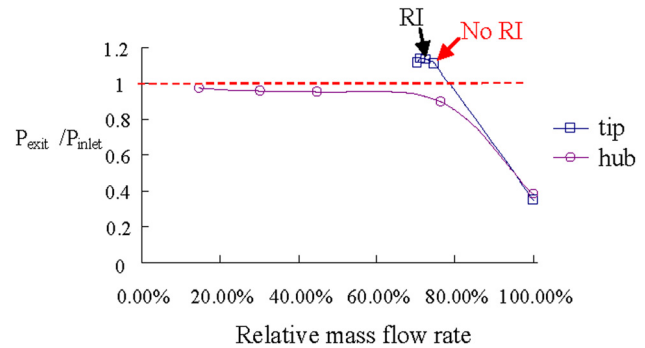


Fig. 23 Rotor pressure ratios with mass flow rates ( $P_{\text{exit}}$  and  $P_{\text{inlet}}$  are taken from the locations shown in Fig. 8(a))

is, on the other hand, of a typical high turning turbine profile with a high camber.

Given these distinctive features in local blading for the two profiles, it would be of interest to examine the overall pressure change characteristics under different flow rates. The experimentally measured pressures for the tip region already showed that when the volumetric flow rate was reduced to a certain level, the tip region locally operates as a compressor. To confirm this observation and to look into its relation to the rotating instability, the tip pressure ratios across the rotor at different flow rates are calculated for both the tip and hub sections.

It can be seen from Fig. 23 that when the mass flow rate goes below 80% of the nominal flow, the tip blade profile produces a pressure rise through the rotor row, meaning that the tip section is now working as a compressor. This behavior of developing a rotating instability when the rotor locally functions as a compressor is qualitatively consistent with the experimental observation. On the other hand, for the hub profile even when the relative mass flow rate is reduced to 15% of the nominal value, the rotor still functions as a turbine. These results indicate that the blade profile has a large influence on the overall pressure characteristics, and more specifically on the onset of rotating instability.

Thus, both the experimental results and the present 2D calculations consistently imply that a compressor mode of the local operation for a turbine blading might be linked to the occurrence of a rotating instability. However, it is also clear that there are operation points on the pressure ratio-mass flow characteristics, where the local operation is in a compressor mode (i.e. pressure ratio  $>1$ ), but no rotating instabilities are observed. In addition, this is also consistently observed in both the experimental results and the present calculations. Therefore, one can come to a more consistent hypothesis based on the results so far: operating as a compressor locally may be a necessary but not sufficient condition for the occurrence of a rotating instability for turbine blading.

Finally it is commented that the rotating instability observed in 2D configurations shows some similarities to the experiment [9]. Although 3D vortical structures associated with a tip clearance flow may be linked to a rotating instability as commonly suggested, the present analysis seems to indicate that they may not necessarily be the cause of the instability. The present results show that under a low mass flow condition, a similar rotating pattern can be produced in a purely 2D blading configuration. The distinctively different characteristics of the tip and hub sections imply that the blading geometry makes a difference in the onset, formation and development of the rotating instability for turbine blades.

## Concluding Remarks

Numerical studies have been conducted to understand the rotating instability previously experimentally identified at low mass flow rates in a model steam turbine last stage. An initial CFD analysis using a time-domain RANS solver is able to capture a



large scale separated flow pattern, which compares well with the experimentally observed one.

To identify the rotating instability phenomenon, further analyses with two distinctively different 2D blade profiles from the model turbine blades are carried out in whole annulus simulations at both the nominal and a range of low mass flow off-design conditions.

The results of the near tip section consistently show that a rotating pattern nonsynchronized with the rotor speed exists at low mass flow conditions. A modal analysis suggests that the circumferential structure of the rotating disturbances is of various wave numbers and the rotating speed of the patterns in the stationary frame of reference is about 90% of the rotor rotation speed.

The near hub section, on the other hand, is much more stable with no clearly identifiable rotating patterns found at low mass flow conditions. The present computational results, consistent with the previous experimental observations, seem to indicate that a tip section working locally as compressor may be a necessary, though not sufficient, condition for a rotating instability to develop in a turbine configuration.

It is recognized that the present simulations of the rotating instabilities are limited by the 2D nature, but they can be used as a reference to understand truly 3D effects on the onset and development of rotating instabilities in steam turbines.

## Acknowledgment

The authors wish to acknowledge Siemens Energy for the financial support and for the permission to publish this work. They also wish to thank the research team in the Institute of Thermal Turbomachinery (ITSM) of the University of Stuttgart for provision of the valuable test data.

## Nomenclature

A = cross-section area,  $m^2$   
 BPF = blade passing frequency  
 Cax = blade chord length in axial direction, m  
 CP = steady pressure coefficient,  $CP = \frac{P_0 - P}{P_0 - P_{ext}}$   
 e = internal energy, J/kg  
 h = enthalpy  
 $P_o$  = total pressure, Pa  
 $P_s$  = static pressure, Pa  
 PS = pressure surface  
 r = radius, m  
 RANS = Reynolds-averaged Navier–Stokes equations  
 RF = rotor rotational frequency  
 RIF = rotational instability frequency  
 SS = suction surface  
 u = axial velocity, m/s  
 $\dot{V}$  = volumetric flow rate,  $m^3/s$   
 v = tangential velocity, m/s  
 w = radial velocity, m/s  
 $\mu$  = dynamic viscosity, Pas  
 $\omega$  = angular frequency, Hz

$\varphi$  = volume flow rate, normalized by rotating speed,

$$\varphi = \frac{(\dot{V}/A)}{\omega r}$$

$\varphi_r$  = relative volume flow rate,  $\varphi_r = \frac{\varphi}{\varphi_{design}}$

$\rho$  = density,  $kg/m^3$

$\Omega$  = angular rotational speed, Hz

## References

- [1] Day, I. J., 1993, "Stall Inception in Axial Flow Compressors," *ASME J. Turbomach.*, **115**(1), pp. 1–9.
- [2] He, L., 1997, "Computational Study of Rotating Stall Inception in Axial Compressors," *AIAA J. Propul. Power*, **13**(1), pp. 31–38.
- [3] Hah, C., Schulze, R., Wagner, S., and Hennecke, D. K., 1999, "Numerical and Experimental Study for the Short Wavelength Stall Inception in a Low-Speed Axial Compressor," Proceedings of the Fourteenth ISABE Conference, Florence, Italy, September 5–10, ISABE Paper No. 99-7033.
- [4] He, L., and Ismael, J. O., 1999, "Computations of Blade Row Stall Inception in Transonic Flows," *Aeronaut. J.*, **103**(1025), pp. 317–324.
- [5] Bent, P. H., McLaughlin, D. K., and Thompson, D. E., 1992, "The Influence of Discharge Configuration on the Generation of Broadband Noise in Centrifugal Turbomachinery," D. DGLR/AIAA Paper No. 92-02-099.
- [6] Mongeau, L., and Quinlan, D. A., 1992, "An Experimental Study of Broadband Noise Sources in Small Axial Fans," Proceedings of the International Symposium on Fan Noise INCE, Senlis, France.
- [7] Mongeau, L., Thompson, D. E., and McLaughlin, D. K., 1993, "Sound Generation by Rotating Stall in Centrifugal Turbomachines," *J. Sound Vib.*, **163**(1), pp. 1–30.
- [8] Cumpsty, N. A., 2004, *Compressor Aerodynamics* 2nd ed., Krieger Publishing Company, Malabar, FL.
- [9] Gerschütz, W., Casey, M., and Truckenmüller, F., 2005, "Experimental Investigations of Rotating Flow Instabilities in the Last Stage of a Low-Pressure Model Steam Turbine During Windage," *Proc. IMechE, Part A: J. Power Energy*, **219**, pp. 499–510.
- [10] Hah, C., Voges, M., Mueller, M., and Schiffer, H. P., 2010, "Characteristics of Tip Clearance Flow Instability in a Transonic Compressor," Proceedings of ASME Turbo Expo 2010: Power for Land, Sea and Air (GT2010), Glasgow, UK, June 14–18, *ASME Paper No. GT2010-22101*, pp. 63–74.
- [11] März, J., Hah, C., and Neise, W., 2002, "An Experimental and Numerical Investigation into the Mechanisms of Rotating Instability," *ASME J. Turbomach.*, **124**(3), pp. 367–374.
- [12] Vo, H. D., 2010, "Role of Tip Clearance Flow in Rotating Instabilities and Non-synchronous Vibrations," *J. Propul. Power*, **26**(3), pp. 556–561.
- [13] Kameier, F., and Neise, W., 1997, "Rotating Blade Flow Instability as a Source of Noise in Axial Turbomachines," *J. Sound Vib.*, **203**(5), pp. 833–853.
- [14] Liu, J. M., Holste, F., and Neise, W., 1996, "On the Azimuthal Mode Structure of Rotating Blade Flow Instabilities in Axial Turbomachines," AIAA Meeting Papers on Disc, A9630853, AIAA Paper No. 96-1741.
- [15] Baumgartner, M., Kameier, F., and Hourmouziadis, J., 1995, "Non-Engine Order Blade Vibration in a High Pressure Compressor," Proceedings of the ISABE-Twelfth International Symposium on Airbreathing Engines, Melbourne, Australia, September 10–15.
- [16] Sparlart, P. R., and Allmaras, S. R., 1992, "A One-Equation Turbulence Model for Aerodynamic Flows," AIAA Paper No. 92-0439.
- [17] Jameson, A., Schmidt, W., and Turkel, E., 1981, "Numerical Solutions of the Euler Equation by Finite Volume Method Using Runge-Kutta Time-Stepping Scheme," AIAA Paper No. 81-1259.
- [18] He, L., 2000, "3-D Navier-Stokes Analysis of Rotor-Stator Interactions in Axial-Flow Turbines," *Proc. IMech. E, Part A*, **214**(1), pp. 13–22.
- [19] He, L., 1998, "Unsteady Flow in Oscillating Turbine Cascades," *ASME J. Turbomach.*, **120**(2), pp. 262–275.
- [20] Truckenmüller, F., 2002, "Untersuchungen zur aerodynamisch induzierten Schwingungsanregung von Niederdruck- Laufschaufeln bei extremer Teillast," Ph.D. thesis, University of Stuttgart, Stuttgart, Germany.
- [21] Denton, J. D., 1992, "The Calculation of Three-Dimensional Viscous Flow Through Multistage Turbomachine," *ASME J. Turbomach.*, **114**(1), pp. 18–26.